PAPER • OPEN ACCESS

Ultracold $^{88}Sr_2$ molecules in the absolute ground state

To cite this article: K H Leung *et al* 2021 *New J. Phys.* **23** 115002

View the article online for updates and enhancements.

New Journal of Physics

The open access journal at the forefront of physics

PAPER

Ultracold ^{88}Sr$_2$ molecules in the absolute ground state

K H Leung[1,*] ⓘ, E Tiberi[1], B Iritani[1], I Majewska[2] ⓘ, R Moszynski[2] and T Zelevinsky[1,*] ⓘ

[1] Department of Physics, Columbia University, 538 West 120th Street, New York, NY 10027-5255, United States of America
[2] Quantum Chemistry Laboratory, Department of Chemistry, University of Warsaw, Pasteura 1, 02-093 Warsaw, Poland
[*] Authors to whom any correspondence should be addressed.

E-mail: kl2908@columbia.edu and tanya.zelevinsky@columbia.edu

Abstract

We report efficient all-optical creation of an ultracold gas of alkaline-earth-metal dimers, ^{88}Sr$_2$, in their absolute ground state. Starting with weakly bound singlet molecules formed by narrow-line photoassociation in an optical lattice, followed by stimulated Raman adiabatic passage (STIRAP) via a singlet-dominant channel in the $(1)0_u^+$ excited potential, we prepare pure samples of more than 5500 molecules in $X^1\Sigma_g^+(v=0,\ J=0)$. We observe two-body collisional loss rates close to the universal limit for both the least bound and most bound vibrational states in $X^1\Sigma_g^+$. We demonstrate the enhancement of STIRAP efficiency in a magic-wavelength optical lattice where thermal decoherence is eliminated. Our results pave the way for the use of alkaline-earth-metal dimers for high-precision spectroscopy, and indicate favorable prospects for robust quantum state preparation of ultracold molecules involving closed-shell atoms, as well as molecule assembly in deep optical traps tuned to a magic wavelength.

1. Introduction

Molecules serve as natural test beds for molecular quantum electrodynamics [1–4], in addition to tests of beyond-standard-model physics such as searches for T-symmetry violation [5–10], dark matter [11–13], time variation of fundamental constants [14–18], and non-Newtonian gravity [19]. In this regard, alkaline-earth-metal molecules represent an exciting frontier since their closed-shell structure lead to $^1\Sigma$ ground potentials that are naturally insensitive to external perturbations. Furthermore, homonuclear combinations possess high-Q subradiant transitions to the excited potentials that can be utilized as *in situ* magnetometers for systematic calibrations. These qualities present a pristine environment for precise molecular spectroscopy as a means to probe new physics. In addition, molecular gases at cold or ultracold temperatures provide experimental benchmarks for understanding collisions and chemical reactions, where accurate theoretical descriptions that include quantum effects remain a significant computational challenge [20–29]. In these applications, often it is necessary to perform tailored state preparation and measurement of the molecules in specific rovibronic and hyperfine states.

On another front, the ability to prepare molecular ensembles with increasingly greater phase-space densities has been driven by efforts to observe novel many-body physics [30–34] and to realize platforms for quantum information processing [35–43] that take advantage of the rich rovibronic structure of molecules. In one approach to the creation of ultracold molecular ensembles, molecules are associated via optical or magnetic Feshbach resonances from laser-cooled ultracold atoms. By preserving the original atomic phase-space density, this has led to the creation of degenerate Bose [44–46] and Fermi [47] alkali-metal diatomic molecular gases. However, in many practical applications, it is advantageous to initialize the molecules in a deeply bound state. For example, in bi-alkalis [48–59], a common step involves de-exciting the weakly bound Feshbach molecules to the absolute ground state using stimulated Raman adiabatic passage (STIRAP) in order to access the large molecule-frame dipole moments. Despite these

technical successes [60] and prior work on weakly-bound molecules of Sr_2 [61–63] and Yb_2 [64], the production of ultracold molecules consisting of closed-shell atoms in the absolute ground state has yet to be demonstrated.

In this paper, we extend the robust state control offered by STIRAP to the entire ground potential of $^{88}Sr_2$, a homonuclear alkaline-earth-metal molecule. This paper is organized into three main parts. First, we describe the spectroscopy and transition strength measurements of the $(1)0_u^+$ and $X^1\Sigma_g^+$ potentials in order to identify a feasible STIRAP pathway for adiabatic transfer within $X^1\Sigma_g^+$. Next, as proof of concept, we experimentally perform STIRAP to create absolute-ground-state molecules and investigate factors that limit the transfer efficiencies both in free flight and in a magic-wavelength optical lattice. Finally, we study the lifetime of the absolute-ground-state molecules and measure the two-body inelastic loss rates to extend our understanding of ultracold collisions, which may potentially inform the feasibility of producing stable molecular Bose–Einstein condensates [65–67]. We expect that the techniques described herein can be generalized to molecules consisting of at least one closed-shell atom [68–73], and to other molecular species in deep optical traps such as tweezers and lattices [74–80].

2. Experimental methods

We employ a standard two-stage magneto-optical trap (MOT) cycling on the broad $^1S_0-^1P_1$ and narrow $^1S_0-^3P_1$ transitions in ^{88}Sr, while repumping on $^3P_2-^3S_1$ and $^3P_0-^3S_1$. This prepares the atoms in the $^1S_0$ electronic ground state at approximately 2(1) μK as inferred from a time-of-flight ballistic expansion. During the narrow-line MOT cooling stage, the atoms are overlapped with a one-dimensional optical lattice with a typical trap depth of 50 μK where they remain optically trapped after the MOT coils are ramped off. In this work, the light for the lattice is derived from a Ti:sapphire laser. To produce weakly bound molecules in the electronic ground potential, $X^1\Sigma_g^+$, we photoassociate the atomic sample with a 1.5 ms laser pulse to $(1)0_u^+(v = -4, J = 1)$ where a sizable fraction subsequently decays down to the least bound vibrational states $X(62, 0)$ and $X(62, 2)$ [63]. In a few instances, we alternatively photoassociate to $(1)0_u^+(-5, 1)$ to produce $X(61, 0)$ and $X(61, 2)$.

The nuclear spin of ^{88}Sr is $I = 0$, resulting in the absence of hyperfine structure. Spin statistics forces the molecular wavefunction to be even upon the exchange of the bosonic nuclei in $^{88}Sr_2$. This implies that only even J (total angular momentum of the molecule) are allowed in the gerade $X^1\Sigma_g^+$, and only odd J are allowed in the ungerade $(1)0_u^+$. Since the total number of bound states in a given potential is not always known *a priori*, in some cases we use negative values for v (the vibrational quantum number) that count down from the dissociation threshold of the respective potentials.

While we typically work with nearly equal mixtures of $J = 0, 2$ ground state molecules, we can perform a purification step that clears away $J = 2$ molecules. This is done by photodissociating $J = 2$ molecules to the $^1S_0 + ^3P_1$ threshold with an additional laser for 1 ms, and blasting the resulting atoms out of the trap with 461 nm laser light near-resonant with $^1S_0-^1P_1$. In either case, we prepare $\sim 10^4$ molecules in $J = 0$ to serve as our spectroscopic signal. We absorption-image the atomic fragments on $^1S_0-^1P_1$ after photodissociating $J = 0$ molecules above the $^1S_0 + ^3P_1$ threshold with a 120 μs pulse. While we usually perform absorption imaging at a slight grazing angle along the lattice direction to maximize the optical depth (and hence the signal-to-noise ratio), for calibration purposes we also take images perpendicular to the lattice direction from which we deduce that the molecules typically fill $\sim$570 lattice sites.

We use diode lasers for both the pump and anti-Stokes STIRAP lasers. The pump laser is stabilized using the Pound–Drever–Hall technique to a high-finesse cavity ($\mathcal{F} > 10^5$, ultralow expansion glass). This phase stability is transferred to the frequency comb spectrum of a low-noise erbium-doped femtosecond fiber laser (FC1500-250-ULN, Menlo Systems GmbH) by referencing the repetition rate to the pump laser. By phase locking the anti-Stokes to the comb, the relative frequency stability of the pump and anti-Stokes is maintained to < 1 kHz (estimated from initial scans of the Raman clock transition $X(62, 0) \rightarrow X(0, 0)$ using these two lasers; the true value is expected to be at the Hz level). The STIRAP lasers pass through a common Glan–Thompson polarizer with a 100 000:1 extinction ratio to drive π-transitions, and co-propagate along the lattice to minimize momentum transfer.

3. High-resolution spectroscopy

Just as for atomic Sr, due to the heavy mass of the strontium nucleus the singlet and triplet electronic states of Sr_2 are strongly mixed by the spin–orbit interaction [82]. This effect is manifest in the relativistic potential $(1)0_u^+$ that asymptotes to the $^1S_0 + ^3P_1$ threshold, which can be identified as the lower branch of the avoided crossing between the $A^1\Sigma_u^+$ and $c^3\Pi_u$ non-relativistic potentials (figure 1(a)). We

Figure 1. One-photon spectroscopy of $(1)0_u^+$. (a) The spin–orbit interaction couples $A^1\Sigma_u^+$ and $c^3\Pi_u$ (dashed and dotted-dashed respectively) in the manifold of excited potentials resulting in the admixed relativistic potentials $(1)0_u^+$ (solid red) and $(2)0_u^+$ (solid blue). Low-lying states of $(1)0_u^+$ present a pathway for adiabatic transfer in the ground potential $X^1\Sigma_g^+$ (solid black). Ω_1 and Ω_2 are the angular Rabi frequencies of the pump and anti-Stokes lasers respectively. For the spectroscopy of $(1)0_u^+$, only the pump laser is present. (b) Binding energies of the first 37 vibrational levels belonging to $(1)0_u^+$ with $J = 1$. The marked change in trend at approximately -1500 cm^{-1} can be attributed to the avoided crossing of the non-relativistic potentials. (c) Transition strengths S to $(1)0_u^+(v = 9 - 20, 1)$ from $X(62, 0)$ (black squares) and $X(61, 0)$ (blue triangles). (d) Measured linewidths of the $(1)0_u^+$ states (black squares). Yellow diamonds are the theory predictions of S and Γ using the Morse/long-range $(1)0_u^+$ potential described in reference [81]. All error bars represent 1σ uncertainties. The binding energies and transition strength values are listed in table A1 in the appendix A.
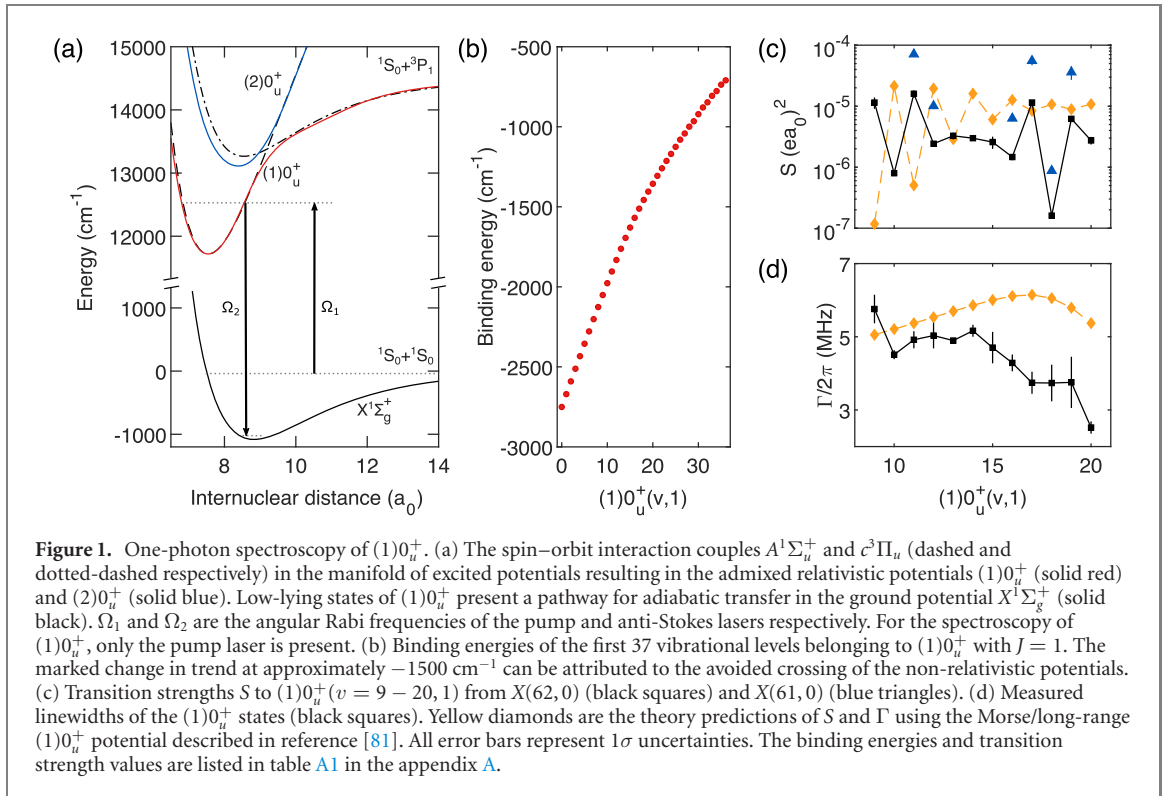
Table 1. Extracted spectroscopic constants of $(1)0_u^+$ in units of cm^{-1}. These were obtained from fitting the 11 lowest bound states to the energies of a vibrating rotor. Since we only measured states of the same angular momentum ($J = 1$), we cannot separate out the vibrational and rotational constants.

Spectroscopic constant	This work	Reference [90]
$-D_e + 2B_e$	$-2791.21(11)$	-2790.90
$\omega_e - 2\alpha_e$	$81.032(47)$	80.713
$\omega_e x_e$	$0.3327(42)$	0.2296

spectroscopically locate the first 37 vibrational levels of $(1)0_u^+$ with $J = 1$ via one-photon excitation of $X(62, 0)$. Previous studies have hitherto only probed weakly bound states near the intercombination [83–89]. As shown in figure 1(b), the effect of the spin–orbit perturbation is markedly noticeable from the change in the trend of the binding energies near -1500 cm^{-1} with respect to the $^1S_0 + ^3P_1$ threshold. Having found the rovibrational ground state of $(1)0_u^+$, we fit the binding energies of the first 11 states to the energies of a vibrating-rotor (valid only for low-lying states)

$$E(v, J) = -D_e + \omega_e \left(v + \frac{1}{2}\right) - \omega_e x_e \left(v + \frac{1}{2}\right)^2 + \left[B_e - \alpha_e \left(v + \frac{1}{2}\right)\right] J(J+1), \tag{1}$$

where ω_e, x_e, B_e, α_e, and D_e are the vibrational, anharmonicity, rotational, and vibration-rotation coupling spectroscopic constants and the potential depth, respectively. Our results, listed in table 1, compares favorably with those quoted for $A^1\Sigma_u^+$ inferred from the observed spectra of several isotopic combinations in reference [90].

For coherent transfer within the singlet $X^1\Sigma_g^+$ ground potential, we ideally require intermediate states with marginal triplet admixture, favorable Frank–Condon overlap with the initial and final states, and a narrow linewidth. In an earlier work [91], we predict that the first two criteria can be satisfied in the vicinity of the $A^1\Sigma_u^+$-$c^3\Pi_u$ avoided crossing, where transitions strengths with mid-to-low-lying states of $X^1\Sigma_g^+$ are expected to be as large as $10^{-2}(ea_0)^2$, while simultaneously maintaining reasonable transition strengths with photoassociated weakly bound molecules. As shown in figures 1(c) and (d), we verify this by measuring the transition strengths of $X(62, 0)$ and $X(61, 0)$ to $(1)0_u^+$ states on both sides of the avoided crossing, as well as their linewidths, Γ. To do so, we follow references [92, 93] and measure the number of remaining molecules after a depletion pulse, $N(\delta_1, t)$, as a function of the pulse time t and angular frequency detuning δ_1 of the

Table 2. Spectroscopic constants for $X^1\Sigma_g^+$ in units of cm^{-1}. The binding energies were determined to an accuracy of < 0.002 cm^{-1}, limited by that of the wavelength meter (High Finesse WS7-60) used to determine the laser frequencies. The rotational splittings have tighter uncertainties because the *relative* precision of the wavemeter is approximately 1×10^{-4} cm^{-1}. For $v = 0$, a frequency comb was used to improve the measurement uncertainty to < 1 MHz. Only the first 8 vibrational levels were used, and the reduced χ^2 of the fits to the binding energies and rotational splittings are 0.69 and 0.94, respectively.

Spectroscopic constant	This work	References [95, 96]
D_e	1081.6395(2)	1081.64(2)
ω_e	40.3210(5)	40.328
$\omega_e x_e$	0.397 88(7)	0.3994
B_e	0.017 577(6)	0.017 58
α_e	1.75(1) $\times 10^{-4}$	1.68 $\times 10^{-4}$

pump laser with respect to the $X \to 0_u^+$ transition. Straightforward rate equations imply that

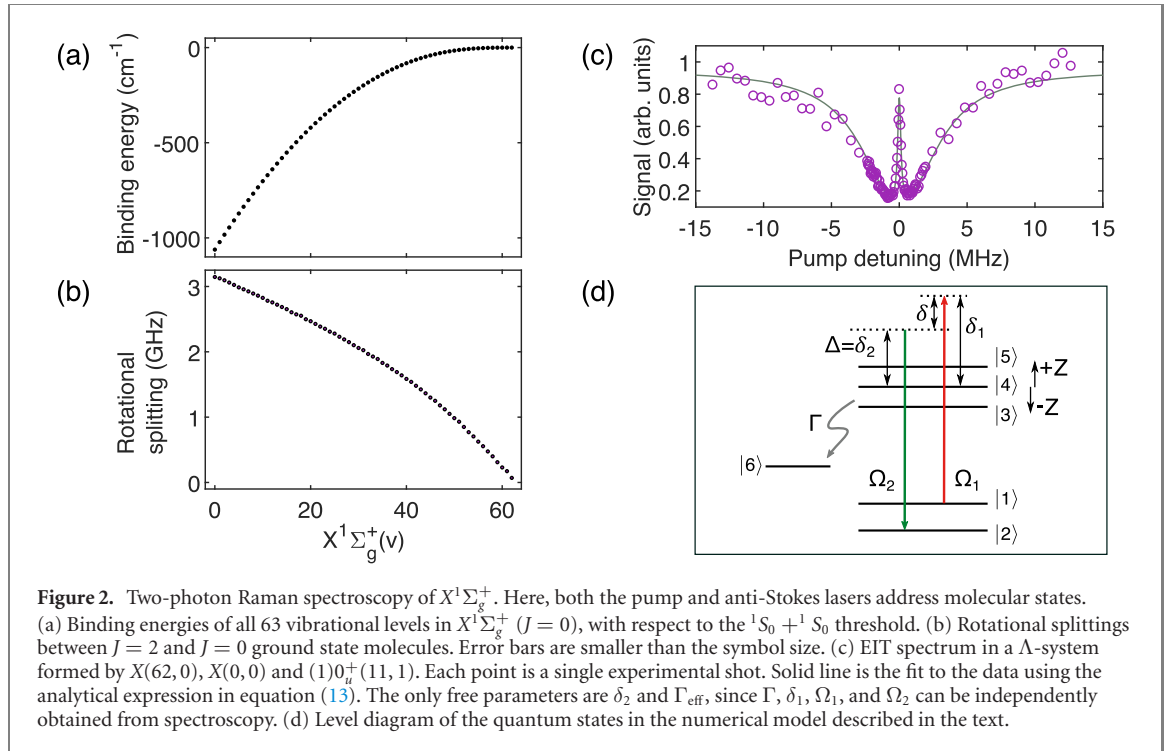$$N(\delta_1, t) = N_0 \, \exp\left[-t\,\Omega_1^2 \frac{\Gamma}{\Gamma^2 + 4\delta_1^2} \right], \tag{2}$$

where N_0 is the initial molecule number and Ω_1 is the angular Rabi frequency of the $X \to 0_u^+$ pump transition. By simultaneously fitting the depletion curves versus t and δ_1, we extract Ω_1 and Γ. We then convert Ω_1 into transition strength, S, from conservative estimates of the pump laser beam waist and power.

Our data suggests that $(1)0_u^+(11, 1)$ offers one of the strongest pump couplings. Moreover, the required laser wavelengths of 793 nm and 732 nm (for the pump and anti-Stokes respectively) to address the entire depth of $X^1\Sigma_g^+$ are within the operating range of commercially available AR-coated laser diodes and our frequency comb. While transitions starting from $X(62, 0)$ are generally weaker than those from $X(61, 0)$, this is outweighed by the fact that we create larger samples of the former and detect them with better efficiency. Thus, in this study we choose $X(62, 0)$ as our initial state and the singlet-dominant $(1)0_u^+(11, 1)$ as the intermediate state for the STIRAP transfer. We note that a similar singlet pathway has been recently shown to be favorable for bi-alkali molecules [94].

To locate the bound states of $X^1\Sigma_g^+$, we perform dark-resonance spectroscopy. We lock the pump laser on resonance with $X(62, 0) \to (1)0_u^+(11, 1)$ and adjust the laser power and pulse time such that we achieve nearly full depletion without bleaching the spectroscopic signal. For this part of the study, we use a tunable Ti:sapphire laser as the anti-Stokes ($\sim$500 W cm^{-2}). On resonance, $(1)0_u^+(11, 1)$ is significantly Stark shifted by the anti-Stokes and the spectroscopic signal is no longer depleted by the pump. In this way, we find all 63 vibrational states in $X^1\Sigma_g^+$ with $J = 0$ and 2, as shown in figures 2(a) and (b). To compare our spectroscopy with Fourier transform spectra in a heatpipe from older studies [95, 96], we note from equation (1) that

$$E(v, 2) - E(v, 0) = 6\left[B_e - \alpha_e \left(v + \frac{1}{2} \right) \right]. \tag{3}$$

By simultaneously fitting the binding energies and the $J = 0, 2$ rotational splittings of the first 8 vibrational levels to equations (1) and (3) respectively, we extract the spectroscopic constants (see table 2) and find excellent agreement with the values reported in references [95, 96] that are weighted across several isotopologues. To verify that the addressed states form a Λ-system, we lock the anti-Stokes laser on resonance with the absolute rovibrational ground state of the ^{88}Sr$_2$ dimer (i.e. $X(0, 0) \to (1)0_u^+(11, 1)$) and reduce its laser power. Sweeping the pump frequency reveals a narrow electromagnetically induced transparency (EIT) peak within the broad single-photon depletion spectrum (see figure 2(c)), heralding the formation of a dark state necessary for STIRAP transfer. At bias magnetic fields of < 1 G the Zeeman sub-levels of $(1)0_u^+(11, 1)$ are essentially unresolved due to the $\sim$5 MHz excited state linewidth, consistent with the expected magnitude of the Zeeman shift [97]. From measurements of Autler–Townes splittings we obtain Ω_2, the angular Rabi frequency of the anti-Stokes coupling for various anti-Stokes laser powers. From a conservative estimate of the anti-Stokes laser beam waist, we find a transition strength of $8.6(9) \times 10^{-2}(ea_0)^2$ for $X(0, 0) \to (1)0_u^+(11, 1)$. This is one of the strongest molecular transitions in ^{88}Sr$_2$, with a value approaching that of a typical atomic transition.

Figure 2. Two-photon Raman spectroscopy of $X^1\Sigma_g^+$. Here, both the pump and anti-Stokes lasers address molecular states. (a) Binding energies of all 63 vibrational levels in $X^1\Sigma_g^+$ ($J=0$), with respect to the $^1S_0 + ^1S_0$ threshold. (b) Rotational splittings between $J=2$ and $J=0$ ground state molecules. Error bars are smaller than the symbol size. (c) EIT spectrum in a Λ-system formed by $X(62,0)$, $X(0,0)$ and $(1)0_u^+(11,1)$. Each point is a single experimental shot. Solid line is the fit to the data using the analytical expression in equation (13). The only free parameters are δ_2 and $\Gamma_{\rm eff}$, since Γ, δ_1, Ω_1, and Ω_2 can be independently obtained from spectroscopy. (d) Level diagram of the quantum states in the numerical model described in the text.

4. STIRAP

4.1. Numerical model

We model the dynamics of the five-level Λ-system (figure 2(d)) with the Lindblad master equation. Here, $|1\rangle, |2\rangle, |3\rangle, |4\rangle, |5\rangle$ represent the states $X(v=62, J=0, m_J=0)$, $X(0,0,0)$, $(1)0_u^+(11,1,-1)$, $(1)0_u^+(11,1,0)$, $(1)0_u^+(11,1,+1)$ respectively, and m_J is the projection of the total angular momentum onto the lab-frame quantization axis $\hat{Z}$. The pump and anti-Stokes electric fields are $\vec{E}_j = \frac{\mathcal{E}_j}{2}\left(\vec{\epsilon}_{(j)}\,{\rm e}^{-{\rm i}\omega_j t} + \vec{\epsilon}^*_{(j)}\,{\rm e}^{+{\rm i}\omega_j t}\right)$ where ω_j are the laser angular frequencies and $j = \{1,2\}$ label the ground states. We pick the convention that the lasers propagate along the positive $\hat{Y}$ direction and write the polarization vectors as

$$\vec{\epsilon}_{(j)} = \hat{Z}\cos\theta_j + \hat{X}{\rm e}^{{\rm i}\phi_j}\sin\theta_j, \tag{4}$$

where the inclination θ with respect to $\hat{Z}$ and the phase ϕ are angles that parameterize the polarization state. The angular Rabi frequencies coupling the ground states to the excited Zeeman sub-levels ($k = \{3,4,5\}$) are $\Omega_{j,k} \equiv \langle k|\vec{d}\cdot\vec{E}_j|j\rangle/\hbar$ where $\vec{d}$ is the dipole moment operator. Since the Clebsch–Gordan coefficients for $J = 0 \leftrightarrow 1$ are independent of m_J, we can write $\Omega_{j,k} = \Omega_j\epsilon_{(j),q}$ where

$$\epsilon_{(j),0} = \cos\theta_j, \quad \epsilon_{(j),\pm1} = \mp\frac{1}{\sqrt{2}}{\rm e}^{{\rm i}\phi_j}\sin\theta_j. \tag{5}$$

Selection rules force $q = -1, 0, +1$ for state labels $k = 3, 4, 5$ respectively. This is true for both $j = 1, 2$ since we have a Λ-system. To make contact with the experiment, we note that the excitation rates and Autler–Townes splittings are both proportional to $\sum_q|\Omega_j\epsilon_{(j),q}|^2 = \Omega_j^2$ which are in turn proportional to the respective laser intensities, so the quantity that we measure in the preceding section is Ω_j even if the polarization is elliptical. Physically, this quantity is equivalent to the Rabi angular frequency for the ideal case of a π-transition ($J = 0 \leftrightarrow 1$, $\Delta m_J = 0$) driven with pure linear polarization exactly parallel to the quantization axis.

In the electric dipole and rotating-wave approximation, the Hamiltonian governing the unitary evolution is [98]

$$H = \begin{pmatrix} \delta_1 & 0 & \Omega_1\epsilon_{(1),-1}/2 & \Omega_1\epsilon_{(1),0}/2 & \Omega_1\epsilon_{(1),+1}/2 & 0 \\ 0 & \delta_2 & \Omega_2\epsilon_{(2),-1}/2 & \Omega_2\epsilon_{(2),0}/2 & \Omega_2\epsilon_{(2),+1}/2 & 0 \\ (\Omega_1\epsilon_{(1),-1})^*/2 & (\Omega_2\epsilon_{(2),-1})^*/2 & -Z & 0 & 0 & 0 \\ (\Omega_1\epsilon_{(1),0})^*/2 & (\Omega_2\epsilon_{(2),0})^*/2 & 0 & 0 & 0 & 0 \\ (\Omega_1\epsilon_{(1),+1})^*/2 & (\Omega_2\epsilon_{(2),+1})^*/2 & 0 & 0 & +Z & 0 \\ 0 & 0 & 0 & 0 & 0 & 0 \end{pmatrix}, \tag{6}$$

where Z is the Zeeman splitting of the excited state, $\delta_j \equiv \omega_j - \omega_0$ are the angular frequency detunings from the $m_J = 0$ sub-level with transition frequency ω_0, and we include an additional auxiliary state $|6\rangle$ that does not participate in the coherent dynamics but merely functions to collect population decay from $|k\rangle$.

To include the relaxation dynamics, we compute

$$\mathcal{L}_k(\rho) = -\frac{1}{2}\{G_k^\dagger G_k, \rho\} + G_k \rho G_k^\dagger, \tag{7}$$

where $\{,\}$ is the anti-commutator, $G_k \equiv \sqrt{\Gamma}|k\rangle\langle 6|$ are the so called *jump operators*, Γ is the excited state linewidth, and ρ is the 6×6 density matrix for the whole system. The effect of $\mathcal{L}_k$ is to generate decay terms proportional to $-\Gamma$ in the diagonals of $|k\rangle$ and $-\Gamma/2$ in the off-diagonals between $|k\rangle$ and $|6\rangle$.

In some cases it is useful to include a phenomelogical decoherence rate Γ_{eff} which can be interpreted as the relative linewidth between the pump and anti-Stokes. To do so we compute

$$\mathcal{D}_{1,2}(\rho) = -\frac{\Gamma_{\text{eff}}}{2}\left(P_1 \rho P_2 + P_2 \rho P_1\right), \tag{8}$$

where $P_j \equiv |j\rangle\langle j|$ are projection operators onto the corresponding diagonal element. The effect of $\mathcal{D}_{1,2}$ is to generate decay terms proportional to $-\Gamma_{\text{eff}}/2$ in the off-diagonals between $|1\rangle$ and $|2\rangle$.

The Lindblad master equation for our system is thus

$$\frac{\mathrm{d}}{\mathrm{d}t}\rho = -\mathrm{i}[H, \rho] + \mathcal{D}_{1,2}(\rho) + \sum_{k=3,4,5}\mathcal{L}_k(\rho), \tag{9}$$

where $[,]$ is the commutator. We numerically solve the time evolution of equation (9) for the input parameters Ω_j, δ_j, θ_j, ϕ_j, Z, Γ, and Γ_{eff}, with the initial condition $\rho_{11}(t=0) = 1$ and zero for all other entries. For later convenience, we define the one-photon (common) detuning $\Delta \equiv \delta_2$, and the two-photon (Raman) detuning $\delta \equiv \delta_1 - \delta_2$.

In the weak probe limit ($\Omega_1 \ll \Omega_2$) such that $\rho_{11} \approx 1$, $\rho_{22} \approx \rho_{33} \approx 0$, we can derive a general analytical expression for the excitation or EIT lineshape. Setting $Z \approx 0$ (unresolved excited states) and discarding negligible terms $O(\Omega_1/\Omega_2)$, we obtain

$$\dot{\rho}_{11} \approx -\sum_k \mathrm{Im}\left(\Omega_{1,k}^* \rho_{1k}\right), \tag{10}$$

$$\dot{\rho}_{1k} \approx \left(-\frac{\Gamma}{2} - i\delta_1\right)\rho_{1k} + i\frac{\Omega_{1,k}}{2} + i\frac{\Omega_{2,k}}{2}\rho_{12} \approx 0,$$

$$\dot{\rho}_{12} \approx \left(-\frac{\Gamma_{\text{eff}}}{2} - i\delta\right)\rho_{12} + i\sum_k \frac{\Omega_{2,k}^*}{2}\rho_{1k} \approx 0.$$

From the first equation, we see that the rate of excitation out of $|1\rangle$ is $R = \sum_k \mathrm{Im}\left(\Omega_{1,k}^* \rho_{1k}\right)$, where $\mathrm{Im}()$ denotes the imaginary part. To find the excitation rate approaching steady-state conditions, we set $\dot{\rho}_{12} \approx \dot{\rho}_{1k} \approx 0$ to solve for ρ_{1k} and substituting back into the expression for R, we find

$$R = \frac{\Gamma}{\Gamma^2 + 4\delta_1^2}$$
$$\times \left[\Omega_1^2 - \left(\sum_k \Omega_{1,k}^* \Omega_{2,k}\right)\left(\sum_k \Omega_{1,k}\Omega_{2,k}^*\right)\frac{\Omega_2^2 - 8\delta\delta_1 + \Gamma_{\text{eff}}\Gamma(1 - 4\delta_1^2/\Gamma^2)}{|\Omega_2^2 + (\Gamma + 2i\delta_1)(\Gamma_{\text{eff}} + 2i\delta)|^2}\right]. \tag{11}$$
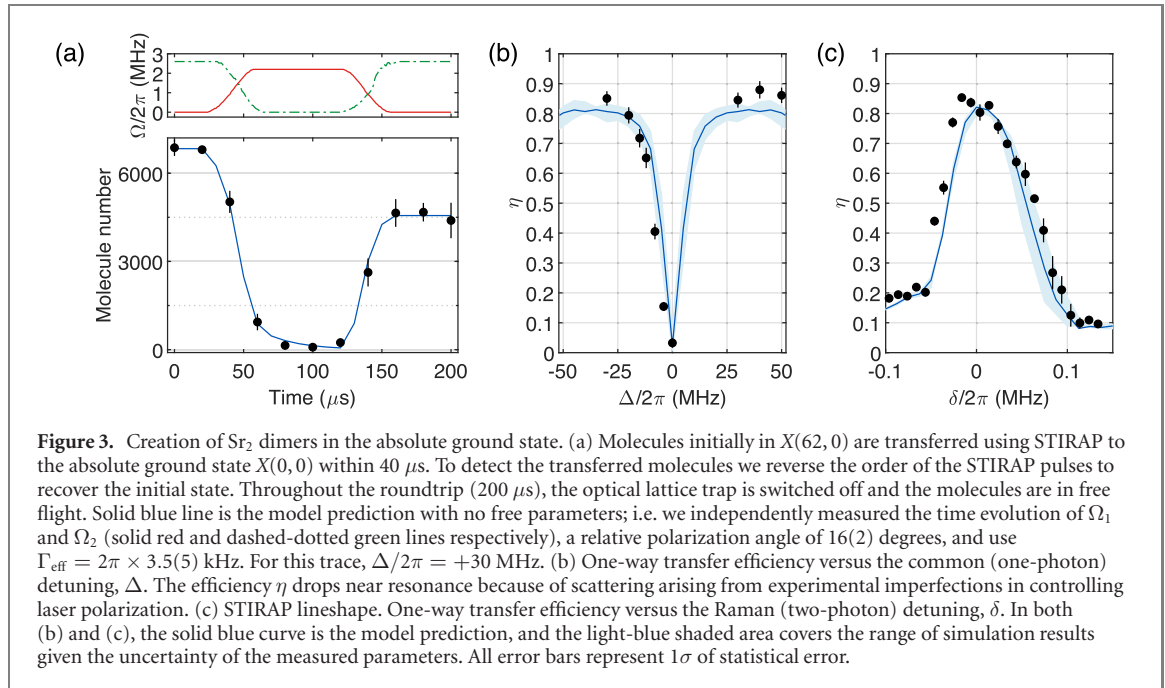
The general EIT lineshape for non-cycling transitions is then

$$N(\delta, \delta_1, t) = N_0 \exp[-Rt]. \tag{12}$$

Finally, for the ideal case where the Raman lasers have exactly the same polarization (i.e. $\theta_1 = \theta_2$, $\phi_1 = \phi_2$), we have $\sum_k \Omega_{1,k}^* \Omega_{2,k} = \sum_k \Omega_{1,k}\Omega_{2,k}^* = \Omega_1\Omega_2$ since both ground states have $J = 0$, and equations (11) and (12) further simplify to

$$N(\delta, \delta_1, t) = N_0 \exp\left[-t\frac{\Gamma\Omega_1^2}{\Gamma^2 + 4\delta_1^2}\left(1 - \Omega_2^2 \frac{\Omega_2^2 - 8\delta\delta_1 + \Gamma_{\text{eff}}\Gamma(1 - 4\delta_1^2/\Gamma^2)}{|\Omega_2^2 + (\Gamma + 2i\delta_1)(\Gamma_{\text{eff}} + 2i\delta)|^2}\right)\right], \tag{13}$$

where the single-photon and two-photon effects are separated into distinct terms; e.g. for $\Omega_2 = 0$, we immediately recover equation (2). Equation (13) can be shown to be in exact agreement with reference [93],
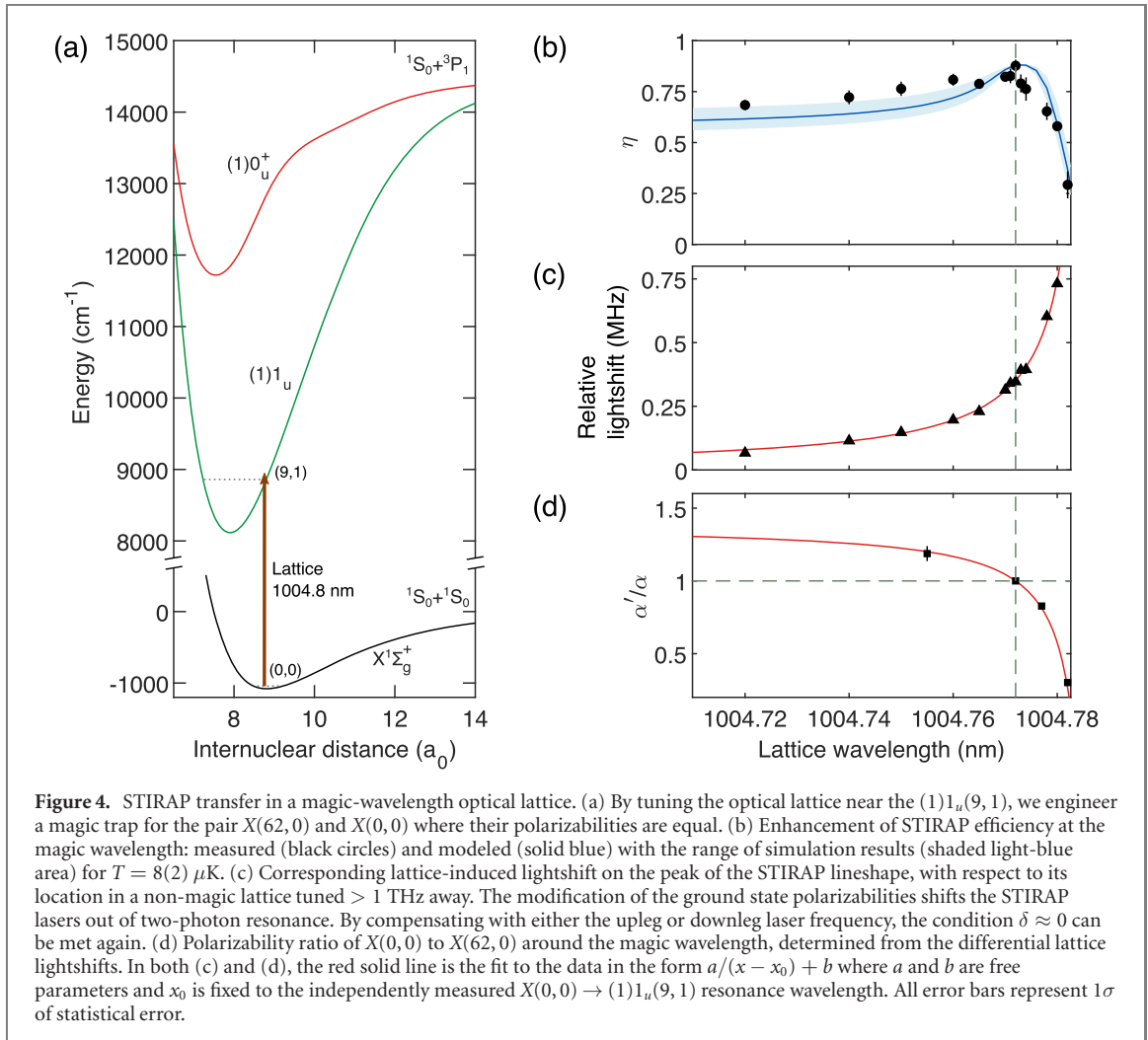
Figure 3. Creation of Sr_2 dimers in the absolute ground state. (a) Molecules initially in $X(62,0)$ are transferred using STIRAP to the absolute ground state $X(0,0)$ within 40 μs. To detect the transferred molecules we reverse the order of the STIRAP pulses to recover the initial state. Throughout the roundtrip (200 μs), the optical lattice trap is switched off and the molecules are in free flight. Solid blue line is the model prediction with no free parameters; i.e. we independently measured the time evolution of Ω_1 and Ω_2 (solid red and dashed-dotted green lines respectively), a relative polarization angle of 16(2) degrees, and use $\Gamma_{eff} = 2\pi \times 3.5(5)$ kHz. For this trace, $\Delta/2\pi = +30$ MHz. (b) One-way transfer efficiency versus the common (one-photon) detuning, Δ. The efficiency η drops near resonance because of scattering arising from experimental imperfections in controlling laser polarization. (c) STIRAP lineshape. One-way transfer efficiency versus the Raman (two-photon) detuning, δ. In both (b) and (c), the solid blue curve is the model prediction, and the light-blue shaded area covers the range of simulation results given the uncertainty of the measured parameters. All error bars represent 1σ of statistical error.

and is also valid in the case where the excited state structure is very well separated such that one effectively addresses a three-level Λ-system. As can be seen in figure 2(c), the analytical form of equation (13) is an excellent fit to the experimental data.

4.2. STIRAP in a non-magic optical lattice

Figure 3(a) shows a representative time evolution of the number of $X(62,0)$ molecules during a roundtrip STIRAP at a common detuning of $\Delta = 2\pi \times 30$ MHz, and angular Rabi frequencies $\Omega_1 = 2\pi \times 2.2$ MHz and $\Omega_2 = 2\pi \times 2.6$ MHz. Here the lattice is tuned to a wavelength of $\lambda = 914.0(1)$ nm, and we perform STIRAP in free flight by switching the lattice trap off for the entirety of the roundtrip to eliminate lattice induced thermal decoherence due to the polarizability difference of $X(62,0)$ and $X(0,0)$. Auxiliary measurements of the molecular cloud size indicate that switching off the trap on timescales of < 200 μs does not result in significant heating or number loss. Moreover, the first order Doppler broadening is expected to be manageable at the level of $f_0\sqrt{3k_B T/M}/c \sim 3.5(5)$ kHz at temperatures of $T = 8(2)$ μK for a Raman transition frequency of $f_0 \approx 31.825$ THz; M is the molecular mass. The roundtrip transfer efficiency is quantified as $\eta^2 = (N_3 - N_2)/N_1$, where N_1, N_3 are the initial and final molecule numbers respectively, and N_2 is the remaining molecule number after the forward transfer. For our Rabi frequencies, we typically achieve full extinction such that $N_2 = 0$, except in a few extreme cases where Δ is very large resulting in reduced adiabaticity. Assuming equal efficiencies for the forward and reverse transfer, we routinely achieve one-way transfer efficiencies of $\eta = 85(3)\%$.

Due to the unresolved Zeeman structure of $(1)0_u^+(11,1)$, a finite relative angle between the polarizations of the Raman (pump and anti-Stokes) lasers dilutes the Rabi couplings and destabilizes the dark state. This leads to increased near-resonant scattering which diminishes the overall transfer efficiencies. In the current study, we measure a relative polarization angle of 16(2) degrees between the pump and anti-Stokes. The cause was traced to a dichroic mirror combining the lasers with the lattice. While we could solve the issue by placing a Glan–Thompson polarizer after this dichroic mirror and immediately before the chamber viewport, geometric constrains in our current setup prohibit this. Nevertheless, for $J = 0 \leftrightarrow 1$ transitions, we can circumvent this by either lifting the degeneracy of Zeeman sublevels, or performing STIRAP at Δ larger than Γ, the linewidth of the $X \to 0_u^+$ transition, as demonstrated in figure 3(b). Numerical simulations using the measured relative polarization angle and expected Γ_{eff} show good agreement. We note that detuned STIRAP has been reported to mitigate other technical imperfections such as laser phase noise and stray reflections [57, 99, 100]. When choosing an operational common detuning, it is prudent to carefully survey the molecular structure. For instance, in $^{88}Sr_2$, the rotational splitting of $X(62,2)$ and $X(62,0)$ is approximately 70 MHz. Therefore, blue detuning is preferred so as to avoid accidental perturbation of the excited state by the pump laser should it be tuned close to $0_u^+(11,1) \to X(62,2)$. Similarly, technical leakage light through the acousto-optic modulators used to modulate the laser intensities can diminish transfer efficiencies should the residual diffraction orders accidentally address a

Figure 4. STIRAP transfer in a magic-wavelength optical lattice. (a) By tuning the optical lattice near the $(1)1_u(9,1)$, we engineer a magic trap for the pair $X(62,0)$ and $X(0,0)$ where their polarizabilities are equal. (b) Enhancement of STIRAP efficiency at the magic wavelength: measured (black circles) and modeled (solid blue) with the range of simulation results (shaded light-blue area) for $T = 8(2)\,\mu$K. (c) Corresponding lattice-induced lightshift on the peak of the STIRAP lineshape, with respect to its location in a non-magic lattice tuned > 1 THz away. The modification of the ground state polarizabilities shifts the STIRAP lasers out of two-photon resonance. By compensating with either the upleg or downleg laser frequency, the condition $\delta \approx 0$ can be met again. (d) Polarizability ratio of $X(0,0)$ to $X(62,0)$ around the magic wavelength, determined from the differential lattice lightshifts. In both (c) and (d), the red solid line is the fit to the data in the form $a/(x - x_0) + b$ where a and b are free parameters and x_0 is fixed to the independently measured $X(0,0) \to (1)1_u(9,1)$ resonance wavelength. All error bars represent 1σ of statistical error.

$X \to 0_u^+$ resonance. These technical effects are non-negligible since the laser intensities used in STIRAP are large.

Figure 3(c) shows the expected asymmetry in the detuned-STIRAP lineshape where the sharper edge faces the one-photon resonance location. The efficiency remains $> 50\%$ even as the relative Raman detuning is scanned over > 100 kHz, and can be widened with larger pump and anti-Stokes laser intensities. Compared to a straightforward Raman π-pulse at similar intensities, STIRAP is robust against small perturbations in laser intensity, laser beam inhomogeneity, and is less susceptible to scattering from the intermediate state.

4.3. STIRAP in a magic lattice

We now explore performing STIRAP in a deep optical lattice, at a trap depth of $U_0 = 1009(44)E_{\rm rec}$. Unlike in the previous subsection, here we leave the trap light on throughout the sequence. Our current strategy for engineering magic lattices involves a lattice blue-detuned from a transition connecting the deeply bound ground state with a narrow rovibronic state in the $(1)1_u$ potential (ungerade, $\Omega = 1$) that asymptotes to the $^1S_0 +\,^3P_1$ threshold [81, 101], as illustrated in figure 4(a). At the magic wavelength, the polarizabilities of the two $J = 0$ vibrational ground states are matched ($\alpha'/\alpha = 1$), resulting in equal trap depths. This effectively removes lattice-induced thermal decoherence and precludes the excitation of breathing modes during the state transfer.

We observe enhancement of STIRAP efficiency in a magic wavelength lattice as shown in figure 4(b), accompanied by lattice-induced Stark shift of the peak STIRAP efficiency (figure 4(c)). To understand this, we measure the polarizability ratio of the ground states at various lattice wavelengths near the $X \to 1_u$ transition (figure 4(d)),

$$\frac{\alpha'}{\alpha} = 1 - 4f_{\rm rec}\frac{L_0}{f_{\rm ax}^2}, \tag{14}$$

where α', α are the scalar polarizabilities of $X(0, 0)$ and $X(62, 0)$ respectively, L_0 is the differential lattice-induced lightshift, f_{ax} is the axial trap frequency (section 5), and $f_{rec} \equiv h/(2M\lambda^2) = E_{rec}/h$ is the standard expression for the recoil frequency. Since L_0 and f_{ax}^2 both depend linearly on lattice intensity, this calculation bypasses the need to determine any geometric parameters (e.g. lattice beam waist).

For $X(0, 0)$, the optimal magic wavelength [81] with the greatest magic detuning ($\Delta_m = 4.493(3)$ GHz) occurs at 1004.7723(1) nm, blue detuned from $X(0, 0) \rightarrow (1)1_u(9, 1)$ with a measured transition strength of $1.33(15) \times 10^{-4}$ $(ea_0)^2$ using an all-frequency method following reference [81]. This is theoretically predicted to be the strongest $X \rightarrow 1_u$ transition that is below the $(1)0_u^+$ potential minimum in $^{88}\text{Sr}_2$. In the Lamb-Dicke regime, the first-order Doppler effect is suppressed ($\Gamma_{eff} = 0$). In general, the lattice-induced differential lightshift on a transition in a non-magic trap becomes compounded for higher trap motional states. For an experimentally set (bare) Raman detuning, δ, of the pump and anti-Stokes for a molecule in the motional ground state, the thermal probability that a molecule is found in an excited motional trap state maps to a probability density, p, for the molecule to experience a Raman detuning *additionally* shifted by $-\delta'$

$$p(-\delta') = \begin{cases} \frac{1}{2}(B\delta')^2 e^{-B\delta'}, & B\delta' \geqslant 0 \\ 0, & B\delta' < 0 \end{cases} \tag{15}$$

where $B \equiv \dfrac{h}{k_B T \left(\sqrt{\alpha'/\alpha} - 1\right)}$ is a factor that depends on the temperature and polarizability mismatch [102]. This probability density $p(-\delta')$ peaks at $\delta'_{max} = 2/B$. To model the transfer efficiencies, we first simulate ideal STIRAP efficiencies, $\eta(\delta)$, for the measured parameters as a function of δ. The function $\eta(\delta)$ peaks at approximately $\delta = 0$. Thus, conceptually the overall efficiency involves an overlap integral between η and p, which we maximize in the actual experiment by manually adjusting the bare Raman detuning (as in figure 4(c)). We can account for this experimental detail to some extent in the model by shifting $\delta' \rightarrow \delta' - \delta'_{max}$ such that the peaks of the distributions p and η line up. The overall efficiency is then calculated as the thermal average of η (i.e. a convolution)

$$\langle \eta \rangle = \frac{\int_{-\infty}^{\infty} d\delta \, \eta(\delta) p(\delta - \delta'_{max})}{\int_{-\infty}^{\infty} d\delta \, p(\delta)}, \tag{16}$$

and the lattice wavelength dependence enters implicitly through α'/α. The solid line in figure 4(b) shows the result of the simulation which reproduces the salient features of the measurement fairly well.

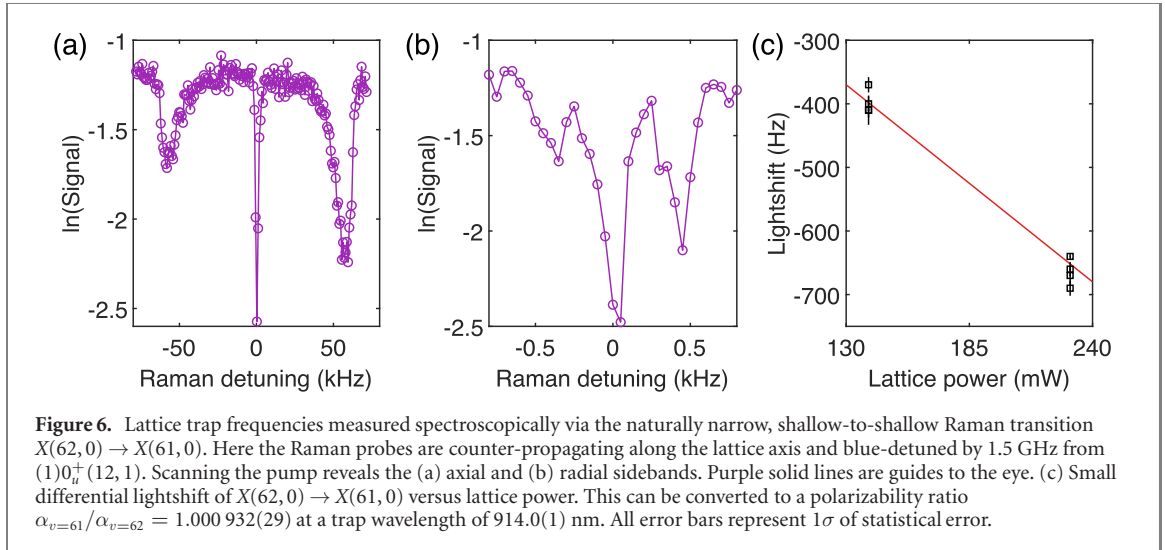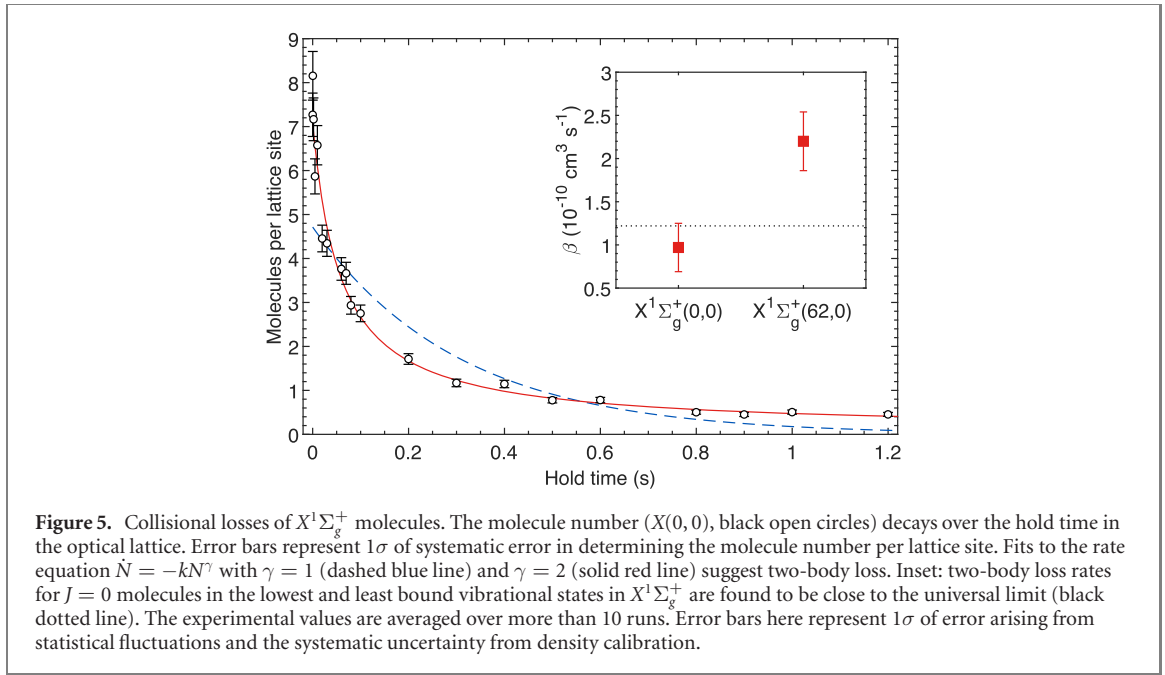## 5. Two-body ultracold reactive collisions

With the creation of large numbers of molecules in $X^1\Sigma_g^+(0, 0)$, we are in a good position to study state-specific losses of an ultracold gas of alkaline-earth-metal dimers. To this end, we prepare a purified sample of $J = 0$ molecules by wiping away $J = 2$ from the initial photoassociated mixture (see section 2). We hold the $v = 0$ ground state molecules after a forward STIRAP sequence in a non-magic optical lattice ($\lambda = 914.0(1)$ nm) for a variable amount of time, and then reverse the STIRAP sequence to recover weakly bound molecules which we detect. Figure 5 shows the decay of the $v = 0$ trapped molecule number over time. Fitted curves to the rate equation $\dot{N} = -kN^\gamma$ (where k is a free parameter) strongly suggest two-body collisions ($\gamma = 2$) to be the dominant loss channel.

We can extract the two-body loss parameter, β, with a density calibration. Following reference [29], the rate equation can be written as
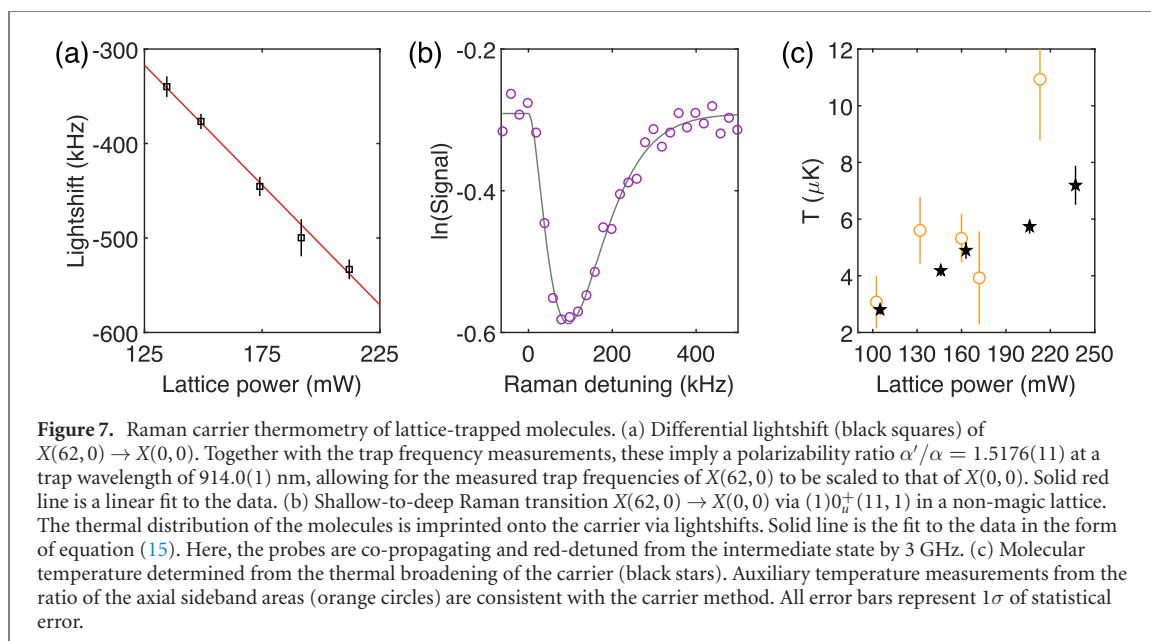
$$\dot{N}(t) = -\beta \frac{A}{T^{3/2}} N(t)^2, \tag{17}$$

where N is the number of molecules per lattice 'pancake', $A \equiv \left(\bar{\omega}^2 M/4\pi k_B\right)^{3/2}$, and $\bar{\omega} \equiv 2\pi (f_{ax} f_{rad}^2)^{1/3}$. To simplify the analysis, in this study we assume that the molecules remain at the same temperature, T, throughout the hold duration.

Since the molecules are tightly trapped in the Lamb-Dicke and resolved sideband regimes, we can spectroscopically access the axial and radial trap frequencies (f_{ax} and f_{rad} respectively) by probing the shallow-to-shallow Raman transition $X(62, 0) \rightarrow X(61, 0)$ via $(1)0_u^+(12, 1)$ as shown in figures 6(a) and (b). Here, we use *counter-propagating* probe beams to maximize the imparted momentum along the axial lattice direction so as to observe the axial sidebands. This Raman transition is nearly magic since the polarizability difference of adjacently bound near-threshold states is negligible (figure 6(c)). As $\bar{\omega}^2$ is measured for $X(62, 0)$, in the case of $X(0, 0)$ we must further scale $\bar{\omega}^2$ by the polarizability ratio α'/α. From measurements of differential lightshift for the shallow-to-deep Raman transition $X(62, 0) \rightarrow X(0, 0)$ (figure 7(a)) and equation (14), we find $\alpha'/\alpha = 1.5176(59)$ at $\lambda = 914.0(1)$ nm.

Figure 5. Collisional losses of $X^1\Sigma_g^+$ molecules. The molecule number ($X(0,0)$, black open circles) decays over the hold time in the optical lattice. Error bars represent 1σ of systematic error in determining the molecule number per lattice site. Fits to the rate equation $\dot{N} = -kN^\gamma$ with $\gamma = 1$ (dashed blue line) and $\gamma = 2$ (solid red line) suggest two-body loss. Inset: two-body loss rates for $J = 0$ molecules in the lowest and least bound vibrational states in $X^1\Sigma_g^+$ are found to be close to the universal limit (black dotted line). The experimental values are averaged over more than 10 runs. Error bars here represent 1σ of error arising from statistical fluctuations and the systematic uncertainty from density calibration.

Figure 6. Lattice trap frequencies measured spectroscopically via the naturally narrow, shallow-to-shallow Raman transition $X(62,0) \rightarrow X(61,0)$. Here the Raman probes are counter-propagating along the lattice axis and blue-detuned by 1.5 GHz from $(1)0_u^+(12,1)$. Scanning the pump reveals the (a) axial and (b) radial sidebands. Purple solid lines are guides to the eye. (c) Small differential lightshift of $X(62,0) \rightarrow X(61,0)$ versus lattice power. This can be converted to a polarizability ratio $\alpha_{v=61}/\alpha_{v=62} = 1.000\,932(29)$ at a trap wavelength of 914.0(1) nm. All error bars represent 1σ of statistical error.

The next step is to determine the temperature of the molecular ensemble. We do so using carrier thermometry [102] with the shallow-to-deep Raman transition $X(62,0) \rightarrow X(0,0)$ and *co-propagating* probes (see figure 7(b)). For the purposes of inferring temperature via thermally imprinted lattice lightshifts (i.e. equation (15)), probing a transition with a large polarizability difference is advantageous and has better accuracy since the effect is exaggerated over other broadening sources (e.g. power broadening) [103]. In figure 7(c) we compare the temperatures extracted using carrier thermometry to the conventional method of taking the ratio of the integrated area under the sidebands and find good agreement.

The measured two-body loss rate coefficient β for $X(0,0)$ and $X(62,0)$ are $0.97(28) \times 10^{-10}$ cm^3 s^{-1} and $2.2(0.3) \times 10^{-10}$ cm^3 s^{-1} respectively, which are found to be unaffected by the presence of $J = 2$ vibrationally least bound molecules. These results are summarized in the inset to figure 5. An estimate of the universal inelastic loss rate via the dominant *s*-wave channel for $X(0,0)$ yield 1.22×10^{-10} cm^3 s^{-1}, independent of the ensemble temperature [104]. This estimate relies on a coupled cluster computation for the isotropic van der Waals coefficient, C_6, using the explicitly connected representation of the expectation value and polarization propagator [105, 106] and the best approximation XCCSD4 method [107]. We find $C_6 = 15\,685$ a.u. for Sr$_2$ dimers at the equilibrium distance $R_e = 8.829a_0$, consistent with an independent calculation from reference [108]. We had previously applied the same method and basis set to calculate the leading van der Waals coefficient for atomic strontium in the ground state and found excellent agreement with high-resolution Fourier transform spectra [82, 96], thus we expect a similar level of accuracy for the absolute ground state strontium molecules in the present investigation. The closeness of our measured β for

Figure 7. Raman carrier thermometry of lattice-trapped molecules. (a) Differential lightshift (black squares) of $X(62, 0) \to X(0, 0)$. Together with the trap frequency measurements, these imply a polarizability ratio $\alpha'/\alpha = 1.5176(11)$ at a trap wavelength of 914.0(1) nm, allowing for the measured trap frequencies of $X(62, 0)$ to be scaled to that of $X(0, 0)$. Solid red line is a linear fit to the data. (b) Shallow-to-deep Raman transition $X(62, 0) \to X(0, 0)$ via $(1)0_u^+(11, 1)$ in a non-magic lattice. The thermal distribution of the molecules is imprinted onto the carrier via lightshifts. Solid line is the fit to the data in the form of equation (15). Here, the probes are co-propagating and red-detuned from the intermediate state by 3 GHz. (c) Molecular temperature determined from the thermal broadening of the carrier (black stars). Auxiliary temperature measurements from the ratio of the axial sideband areas (orange circles) are consistent with the carrier method. All error bars represent 1σ of statistical error.

$X(0, 0)$ molecules to the universal loss limit suggests that the molecules react with near unity probability following a collision at short range. For a homonuclear alkaline-earth dimer in the absolute ground state, one possible exoergic process that will manifest in such a loss is the formation of stable trimers [108]. Another possibility is the photoexcitation of 'sticky' four-body complexes by the intense lattice light [109, 110]. For the near-threshold $X(62, 0)$ state, the slightly larger loss rate may indicate that vibrational relaxation effects are non-negligible. The results, however, do not limit the prospects of using these molecules for precision spectroscopy, since the implementation of a 3D lattice can strongly suppress collisional losses and enable long interrogation times [111].

6. Conclusion

In summary, we have created ultracold ^{88}Sr$_2$ molecules in the absolute ground state using STIRAP to coherently transfer photoassociated molecules. We achieve favorable transfer efficiencies of nearly 90%, both in free flight and in a deep optical lattice tuned to a magic wavelength, limited by the available pump laser power. Future experiments should benefit from a redesigned experimental setup such that the relative polarization of the pump and anti-Stokes beams can be made more parallel. We have mapped out all 63 vibrational states with $J = 0, 2$ in $X^1\Sigma_g^+$ to an accuracy of 0.002 cm^{-1}. We spectroscopically observed the effect of spin–orbit coupling on the bound states of $(1)0_u^+$, verified its potential depth, and identified a favorable STIRAP pathway from the measured transition strengths. We investigated the lifetime of absolute ground state molecules in an optical trap and find two-body collisions near the universal loss rate.

The work presented here demonstrates the ability to access the full vibrational state space of $X^1\Sigma_g^+$ closed-shell molecules, and in doing so, opens up the variety of experiments where efficient state initialization in a deeply bound level is necessary. The $X \to 1_u$ transition described here presents one of the most favorable conditions for engineering a near-resonant magic lattice for Raman transitions within the ground potential, so as a natural next step we plan to utilize this to explore the stability and accuracy of the vibrational molecular clock. Large samples of ground state molecules should allow us to gain insight into the photon scattering process in a near-resonant magic lattice [101], and enable loading into 3D magic lattices at mid-IR wavelengths tuned far below the minima of the excited potentials where we expect the main loss processes to be diminished. With these, tests of fundamental physics with alkaline-earth-metal molecules are now within reach.

Acknowledgments

Table A1. Binding energies for the lowest 37 vibrational states of $(1)0_u^+$ with $J = 1$ with respect to the atomic threshold $^1S_0 + ^3P_1$. Also shown are $S_{X(62,0)}$ and $S_{X(61,0)}$, the measured $X \to 0_u^+$ transition strengths from $X(62, 0)$ and $X(61, 0)$ respectively, in units of $(10^{-5}(ea_0)^2)$. These values are plotted in figure 1. All reported values are obtained in this work.

$(1)0_u^+(v, J = 1)$	Binding energy (MHz)	$S_{X(62,0)}$	$S_{X(61,0)}$
0	82 462 408(60)	—	—
1	80 056 883(60)	—	—
2	77 669 758(60)	—	—
3	75 301 073(60)	—	—
4	72 950 983(60)	—	—
5	70 619 778(60)	—	—
6	68 307 898(60)	—	—
7	66 016 088(60)	—	—
8	63 745 468(60)	—	—
9	61 497 833.94(12)	1.15(24)	—
10	59 275 910.26(35)	0.0797(84)	—
11	57 084 156.51(12)	1.60(23)	7.10(10)
12	54 929 909.90(11)	0.242(20)	1.01(11)
13	52 825 770.430(40)	0.327(42)	—
14	50 791 292.56(10)	0.300(16)	—
15	48 855 512.13(18)	0.258(58)	—
16	47 036 183.94(23)	0.147(17)	0.630(67)
17	45 320 332.03(14)	1.15(12)	5.54(84)
18	43 686 692.340(90)	0.0161(12)	0.0873(92)
19	42 124 534.970(70)	0.620(66)	3.60(90)
20	40 655 031.210(80)	0.274(39)	—
21	39 174 338(60)	—	—
22	37 763 228(60)	—	—
23	36 377 628(60)	—	—
24	35 066 118(60)	—	—
25	33 737 818(60)	—	—
26	32 397 458(60)	—	—
27	31 241 318(60)	—	—
28	29 959 413(60)	—	—
29	28 947 228(60)	—	—
30	27 621 073(60)	—	—
31	26 361 623(60)	—	—
32	25 400 438(60)	—	—
33	24 186 203(60)	—	—
34	23 295 548(60)	—	—
35	22 096 778(60)	—	—
36	21 284 598(60)	—	—

Appendix A. $(1)0_u^+$ binding energies and transition strengths

Table A1 shows the binding energies for the lowest 37 vibrational states of $(1)0_u^+$ with $J = 1$ via laser excitation from $X(62, 0)$, with respect to the atomic threshold $^1S_0 + ^3P_1$. We take the intercombination frequency from reference [112] and the binding energy of $X(62, 0)$ from reference [89].

For $v = 9$–20 we use a frequency comb to determine the pump laser frequency to a high precision. The $X \to 0_u^+$ resonance frequencies are linearly extrapolated to zero lattice intensity, and we report uncertainties inflated by the square root of the reduced χ^2 if it is greater than unity. The rest were determined using a wavelength meter to an uncertainty of 60 MHz.

In addition, we also list $S_{X(62,0)}$ and $S_{X(61,0)}$, the measured $X \to 0_u^+$ transition strengths from $X(62, 0)$ and $X(61, 0)$ respectively. The method of determining these transition strengths is described in the main text.

ORCID iDs

K H Leung ⓘ https://orcid.org/0000-0002-9436-5312
I Majewska ⓘ https://orcid.org/0000-0001-9276-7628
T Zelevinsky ⓘ https://orcid.org/0000-0003-3682-4901

References

[1] Alighanbari S, Giri G S, Constantin F L, Korobov V I and Schiller S 2020 Precise test of quantum electrodynamics and determination of fundamental constants with HD^+ ions *Nature* **581** 152–8

[2] Lai K F, Czachorowski P, Schlösser M, Puchalski M, Komasa J, Pachucki K, Ubachs W and Salumbides E J 2019 Precision tests of nonadiabatic perturbation theory with measurements on the DT molecule *Phys. Rev. Res.* **1** 033124

[3] Patra S *et al* 2020 Proton–electron mass ratio from laser spectroscopy of HD^+ at the part-per-trillion level *Science* **369** 1238–41

[4] Kortunov I V, Alighanbari S, Hansen M G, Giri G S, Korobov V I and Schiller S 2021 Proton–electron mass ratio by high-resolution optical spectroscopy of ion ensembles in the resolved-carrier regime *Nat. Phys.* **17** 569–73

[5] Andreev V *et al* 2018 Improved limit on the electric dipole moment of the electron *Nature* **562** 355–60

[6] Kozyryev I and Hutzler N R 2017 Precision measurement of time-reversal symmetry violation with laser-cooled polyatomic molecules *Phys. Rev. Lett.* **119** 133002

[7] Denis M, Haase P A B, Timmermans R G E, Eliav E, Hutzler N R and Borschevsky A 2019 Enhancement factor for the electric dipole moment of the electron in the BaOH and YbOH molecules *Phys. Rev. A* **99** 042512

[8] Yu P and Hutzler N R 2021 Probing fundamental symmetries of deformed nuclei in symmetric top molecules *Phys. Rev. Lett.* **126** 023003

[9] Ho C J *et al* 2020 New techniques for a measurement of the electron's electric dipole moment *New J. Phys.* **22** 053031

[10] Grasdijk J O *et al* 2021 CeNTREX: a new search for time-reversal symmetry violation in the ^{205}Tl nucleus *Quantum Sci. Technol.* **6** 044007

[11] Kozyryev I, Lasner Z and Doyle J M 2021 Enhanced sensitivity to ultralight bosonic dark matter in the spectra of the linear radical SrOH *Phys. Rev. A* **103** 043313

[12] Roussy T S *et al* 2021 Experimental constraint on axionlike particles over seven orders of magnitude in mass *Phys. Rev. Lett.* **126** 171301

[13] Antypas D, Tretiak O, Zhang K, Garcon A, Perez G, Kozlov M G, Schiller S and Budker D 2021 Probing fast oscillating scalar dark matter with atoms and molecules *Quantum Sci. Technol.* **6** 034001

[14] Kobayashi J, Ogino A and Inouye S 2019 Measurement of the variation of electron-to-proton mass ratio using ultracold molecules produced from laser-cooled atoms *Nat. Commun.* **10** 3771

[15] Truppe S, Hendricks R, Tokunaga S, Lewandowski H, Kozlov M, Henkel C, Hinds E and Tarbutt M 2013 A search for varying fundamental constants using hertz-level frequency measurements of cold CH molecules *Nat. Commun.* **4** 1–7

[16] Bagdonaite J, Jansen P, Henkel C, Bethlem H L, Menten K M and Ubachs W 2013 A stringent limit on a drifting proton-to-electron mass ratio from alcohol in the early universe *Science* **339** 46–8

[17] Shelkovnikov A, Butcher R J, Chardonnet C and Amy-Klein A 2008 Stability of the proton-to-electron mass ratio *Phys. Rev. Lett.* **100** 150801

[18] Hudson E R, Lewandowski H J, Sawyer B C and Ye J 2006 Cold molecule spectroscopy for constraining the evolution of the fine structure constant *Phys. Rev. Lett.* **96** 143004

[19] Borkowski M, Buchachenko A A, Ciuryło R, Julienne P S, Yamada H, Kikuchi Y, Takasu Y and Takahashi Y 2019 Weakly bound molecules as sensors of new gravitylike forces *Sci. Rep.* **9** 14807

[20] Heazlewood B R and Softley T P 2021 Towards chemistry at absolute zero *Nat. Rev. Chem.* 1–16

[21] Krems R V 2008 Cold controlled chemistry *Phys. Chem. Chem. Phys.* **10** 4079–92

[22] Jurgilas S *et al* 2021 Collisions between ultracold molecules and atoms in a magnetic trap *Phys. Rev. Lett.* **126** 153401

[23] Liu Y, Hu M-G, Nichols M A, Yang D, Xie D, Guo H and Ni K-K 2021 Precision test of statistical dynamics with state-to-state ultracold chemistry *Nature* **593** 379–84

[24] Hu M-G, Liu Y, Nichols M A, Zhu L, Quéméner G, Dulieu O and Ni K-K 2021 Nuclear spin conservation enables state-to-state control of ultracold molecular reactions *Nat. Chem.* **13** 435–40

[25] Wolf J, Deiß M, Krükow A, Tiemann E, Ruzic B P, Wang Y, D'Incao J P, Julienne P S and Denschlag J H 2017 State-to-state chemistry for three-body recombination in an ultracold rubidium gas *Science* **358** 921–4

[26] Segev Y, Pitzer M, Karpov M, Akerman N, Narevicius J and Narevicius E 2019 Collisions between cold molecules in a superconducting magnetic trap *Nature* **572** 189–93

[27] Sawyer B C *et al* 2011 Cold heteromolecular dipolar collisions *Phys. Chem. Chem. Phys.* **13** 19059–66

[28] Guo M, Ye X, He J, Quéméner G and Wang D 2018 High-resolution internal state control of ultracold ^{23}Na^{87}Rb molecules *Phys. Rev. A* **97** 020501

[29] Guo M, Ye X, He J, González-Martínez M L, Vexiau R, Quéméner G and Wang D 2018 Dipolar collisions of ultracold ground-state bosonic molecules *Phys. Rev. X* **8** 041044

[30] Micheli A, Brennen G K and Zoller P 2006 A toolbox for lattice-spin models with polar molecules *Nat. Phys.* **2** 341–7

[31] Yi S, Li T and Sun C P 2007 Novel quantum phases of dipolar Bose gases in optical lattices *Phys. Rev. Lett.* **98** 260405

[32] Capogrosso-Sansone B, Trefzger C, Lewenstein M, Zoller P and Pupillo G 2010 Quantum phases of cold polar molecules in 2D optical lattices *Phys. Rev. Lett.* **104** 125301

[33] Gadway B and Yan B 2016 Strongly interacting ultracold polar molecules *J. Phys. B: At. Mol. Opt. Phys.* **49** 152002

[34] Blackmore J A *et al* 2018 Ultracold molecules for quantum simulation: rotational coherences in CaF and RbCs *Quantum Sci. Technol.* **4** 014010

[35] Ni K-K, Rosenband T and Grimes D D 2018 Dipolar exchange quantum logic gate with polar molecules *Chem. Sci.* **9** 6830–8

[36] Hudson E R and Campbell W C 2018 Dipolar quantum logic for freely rotating trapped molecular ions *Phys. Rev. A* **98** 040302

[37] Yu P, Cheuk L W, Kozyryev I and Doyle J M 2019 A scalable quantum computing platform using symmetric-top molecules *New J. Phys.* **21** 093049

[38] Sawant R, Blackmore J A, Gregory P D, Mur-Petit J, Jaksch D, Aldegunde J, Hutson J M, Tarbutt M R and Cornish S L 2020 Ultracold polar molecules as qubits *New J. Phys.* **22** 013027

[39] Lin Y, Leibrandt D R, Leibfried D and Chou C-w 2020 Quantum entanglement between an atom and a molecule *Nature* **581** 273–7

[40] Albert V V, Covey J P and Preskill J 2020 Robust encoding of a qubit in a molecule *Phys. Rev. X* **10** 031050

[41] Campbell W C and Hudson E R 2020 Dipole-phonon quantum logic with trapped polar molecular ions *Phys. Rev. Lett.* **125** 120501

[42] Hughes M *et al* 2020 Robust entangling gate for polar molecules using magnetic and microwave fields *Phys. Rev.* A **101** 062308

[43] DeMille D 2002 Quantum computation with trapped polar molecules *Phys. Rev. Lett.* **88** 067901

[44] Greiner M, Regal C A and Jin D S 2003 Emergence of a molecular Bose–Einstein condensate from a Fermi gas *Nature* **426** 537–40

[45] Jochim S, Bartenstein M, Altmeyer A, Hendl G, Riedl S, Chin C, Hecker Denschlag J and Grimm R 2003 Bose–Einstein condensation of molecules *Science* **302** 2101–3

[46] Zwierlein M W, Stan C A, Schunck C H, Raupach S M F, Gupta S, Hadzibabic Z and Ketterle W 2003 Observation of Bose–Einstein condensation of molecules *Phys. Rev. Lett.* **91** 250401

[47] De Marco L, Valtolina G, Matsuda K, Tobias W G, Covey J P and Ye J 2019 A degenerate Fermi gas of polar molecules *Science* **363** 853–6

[48] Danzl J G, Haller E, Gustavsson M, Mark M J, Hart R, Bouloufa N, Dulieu O, Ritsch H and Nägerl H-C 2008 Quantum gas of deeply bound ground state molecules *Science* **321** 1062–6

[49] Ni K-K *et al* 2008 A high phase-space-density gas of polar molecules *Science* **322** 231–5

[50] Aikawa K, Akamatsu D, Hayashi M, Oasa K, Kobayashi J, Naidon P, Kishimoto T, Ueda M and Inouye S 2010 Coherent transfer of photoassociated molecules into the rovibrational ground state *Phys. Rev. Lett.* **105** 203001

[51] Danzl J G, Mark M J, Haller E, Gustavsson M, Hart R, Aldegunde J, Hutson J M and Nägerl H-C 2010 An ultracold high-density sample of rovibronic ground-state molecules in an optical lattice *Nat. Phys.* **6** 265–70

[52] Takekoshi T, Reichsöllner L, Schindewolf A, Hutson J M, Le Sueur C R, Dulieu O, Ferlaino F, Grimm R and Nägerl H-C 2014 Ultracold dense samples of dipolar RbCs molecules in the rovibrational and hyperfine ground state *Phys. Rev. Lett.* **113** 205301

[53] Molony P K, Gregory P D, Ji Z, Lu B, Köppinger M P, Le Sueur C R, Blackley C L, Hutson J M and Cornish S L 2014 Creation of ultracold ^{87}Rb^{133}Cs molecules in the rovibrational ground state *Phys. Rev. Lett.* **113** 255301

[54] Park J W, Will S A and Zwierlein M W 2015 Ultracold dipolar gas of Fermionic ^{23}Na^{40}K molecules in their absolute ground state *Phys. Rev. Lett.* **114** 205302

[55] Guo M *et al* 2016 Creation of an ultracold gas of ground-state dipolar ^{23}Na^{87}Rb molecules *Phys. Rev. Lett.* **116** 205303

[56] Rvachov T M, Son H, Sommer A T, Ebadi S, Park J J, Zwierlein M W, Ketterle W and Jamison A O 2017 Long-lived ultracold molecules with electric and magnetic dipole moments *Phys. Rev. Lett.* **119** 143001

[57] Seeßelberg F, Buchheim N, Lu Z K, Schneider T, Luo X Y, Tiemann E, Bloch I and Gohle C 2018 Modeling the adiabatic creation of ultracold polar ^{23}Na^{40}K molecules *Phys. Rev.* A **97** 013405

[58] Liu L, Zhang D-C, Yang H, Liu Y-X, Nan J, Rui J, Zhao B and Pan J-W 2019 Observation of interference between resonant and detuned STIRAP in the adiabatic creation of ^{23}Na^{40}K molecules *Phys. Rev. Lett.* **122** 253201

[59] Voges K K, Gersema P, Meyer zum Alten Borgloh M, Schulze T A, Hartmann T, Zenesini A and Ospelkaus S 2020 Ultracold gas of bosonic ^{23}Na^{39}K ground-state molecules *Phys. Rev. Lett.* **125** 083401

[60] Bergmann K *et al* 2019 Roadmap on STIRAP applications *J. Phys. B: At. Mol. Opt. Phys.* **52** 202001

[61] Ciamei A, Bayerle A, Chen C C, Pasquiou B and Schreck F 2017 Efficient production of long-lived ultracold Sr$_2$ molecules *Phys. Rev.* A **96** 013406

[62] Stellmer S, Pasquiou B, Grimm R and Schreck F 2012 Creation of ultracold Sr$_2$ molecules in the electronic ground state *Phys. Rev. Lett.* **109** 115302

[63] Reinaudi G, Osborn C B, McDonald M, Kotochigova S and Zelevinsky T 2012 Optical production of stable ultracold ^{88}Sr$_2$ molecules *Phys. Rev. Lett.* **109** 115303

[64] Borkowski M, Buchachenko A A, Ciuryło R, Julienne P S, Yamada H, Kikuchi Y, Takahashi K, Takasu Y and Takahashi Y 2017 Beyond-Born–Oppenheimer effects in sub-kHz-precision photoassociation spectroscopy of ytterbium atoms *Phys. Rev.* A **96** 063405

[65] Ciamei A, Bayerle A, Pasquiou B and Schreck F 2017 Observation of Bose-enhanced photoassociation products *Europhys. Lett.* **119** 46001

[66] Heinzen D J, Wynar R, Drummond P D and Kheruntsyan K V 2000 Superchemistry: dynamics of coupled atomic and molecular Bose–Einstein condensates *Phys. Rev. Lett.* **84** 5029

[67] Stellmer S, Grimm R and Schreck F 2013 Production of quantum-degenerate strontium gases *Phys. Rev.* A **87** 013611

[68] Barbé V, Ciamei A, Pasquiou B, Reichsöllner L, Schreck F, Żuchowski P S and Hutson J M 2018 Observation of Feshbach resonances between alkali and closed-shell atoms *Nat. Phys.* **14** 881–4

[69] Roy R, Shrestha R, Green A, Gupta S, Li M, Kotochigova S, Petrov A and Yuen C H 2016 Photoassociative production of ultracold heteronuclear YbLi∗ molecules *Phys. Rev.* A **94** 033413

[70] Green A, Li H, See Toh J H, Tang X, McCormick K C, Li M, Tiesinga E, Kotochigova S and Gupta S 2020 Feshbach resonances in *p*-wave three-body recombination within Fermi–Fermi mixtures of open-shell ^{6}Li and closed-shell ^{173}Yb atoms *Phys. Rev.* X **10** 031037

[71] Green A, See Toh J H, Roy R, Li M, Kotochigova S and Gupta S 2019 Two-photon photoassociation spectroscopy of the $^2\Sigma^+$ YbLi molecular ground state *Phys. Rev.* A **99** 063416

[72] Guttridge A, Frye M D, Yang B C, Hutson J M and Cornish S L 2018 Two-photon photoassociation spectroscopy of CsYb: ground-state interaction potential and interspecies scattering lengths *Phys. Rev.* A **98** 022707

[73] Yang B C, Frye M D, Guttridge A, Aldegunde J, Żuchowski P S, Cornish S L and Hutson J M 2019 Magnetic Feshbach resonances in ultracold collisions between Cs and Yb atoms *Phys. Rev.* A **100** 022704

[74] Cairncross W B, Zhang J T, Picard L R B, Yu Y, Wang K and Ni K-K 2021 Assembly of a rovibrational ground state molecule in an optical tweezer *Phys. Rev. Lett.* **126** 123402

[75] He X *et al* 2020 Coherently forming a single molecule in an optical trap *Science* **370** 331–5

[76] Anderegg L, Cheuk L W, Bao Y, Burchesky S, Ketterle W, Ni K-K and Doyle J M 2019 An optical tweezer array of ultracold molecules *Science* **365** 1156–8

[77] Langin T K, Jorapur V, Zhu Y, Wang Q and DeMille D 2021 Polarization enhanced deep optical dipole trapping of λ-cooled polar molecules (arXiv:2106.00622)

[78] Brooks R V, Spence S, Guttridge A, Alampounti A, Rakonjac A, McArd L A, Hutson J M and Cornish S L 2021 Preparation of one ^{87}Rb and one ^{133}Cs atom in a single optical tweezer *New J. Phys.* **23** 065002

[79] Guan Q, Cornish S L and Kotochigova S 2021 Magic conditions for multiple rotational states of bialkali molecules in optical lattices *Phys. Rev.* A **103** 043311

[80] Wu Y, Burau J J, Mehling K, Ye J and Ding S 2021 High phase-space density of laser-cooled molecules in an optical lattice (arXiv:2107.06422)

[81] Leung K H, Majewska I, Bekker H, Lee C-H, Tiberi E, Kondov S S, Moszynski R and Zelevinsky T 2020 Transition strength measurements to guide magic wavelength selection in optically trapped molecules *Phys. Rev. Lett.* **125** 153001

[82] Skomorowski W, Pawłowski F, Koch C P and Moszynski R 2012 Rovibrational dynamics of the strontium molecule in the $A^1\Sigma_u^+$, $c^3\Pi_u$, and $a^3\Sigma_u^+$ manifold from state-of-the-art *ab initio* calculations *J. Chem. Phys.* **136** 194306

[83] Borkowski M, Morzyński P, Ciuryło R, Julienne P S, Yan M, DeSalvo B J and Killian T C 2014 Mass scaling and nonadiabatic effects in photoassociation spectroscopy of ultracold strontium atoms *Phys. Rev.* A **90** 032713

[84] Reschovsky B J, Ruzic B P, Miyake H, Pisenti N C, Julienne P S and Campbell G K 2018 Narrow-line photoassociation spectroscopy and mass-scaling of bosonic strontium (arXiv:1808.06507)

[85] Zelevinsky T, Boyd M M, Ludlow A D, Ido T, Ye J, Ciuryło R, Naidon P and Julienne P S 2006 Narrow line photoassociation in an optical lattice *Phys. Rev. Lett.* **96** 203201

[86] McGuyer B H, McDonald M, Iwata G Z, Tarallo M G, Grier A T, Apfelbeck F and Zelevinsky T 2015 High-precision spectroscopy of ultracold molecules in an optical lattice *New J. Phys.* **17** 055004

[87] McGuyer B H, McDonald M, Iwata G Z, Skomorowski W, Moszynski R and Zelevinsky T 2015 Control of optical transitions with magnetic fields in weakly bound molecules *Phys. Rev. Lett.* **115** 053001

[88] McGuyer B H, McDonald M, Iwata G Z, Tarallo M G, Skomorowski W, Moszynski R and Zelevinsky T 2015 Precise study of asymptotic physics with subradiant ultracold molecules *Nat. Phys.* **11** 32−6

[89] McDonald M 2017 *High precision Optical Spectroscopy and Quantum State Selected Photodissociation of Ultracold $^{88}Sr_2$ Molecules in an Optical Lattice* (Berlin: Springer)

[90] Stein A, Knöckel H and Tiemann E 2011 The states $1^1\Sigma_u^+$, $1^1\Pi_u$ and $2^1\Sigma_u^+$ of Sr_2 studied by Fourier-transform spectroscopy *Eur. Phys. J.* D **64** 227−38

[91] Skomorowski W, Moszynski R and Koch C P 2012 Formation of deeply bound ultracold Sr_2 molecules by photoassociation near the $^1S + {}^3P_1$ intercombination line *Phys. Rev.* A **85** 043414

[92] Guo M, Vexiau R, Zhu B, Lu B, Bouloufa-Maafa N, Dulieu O and Wang D 2017 High-resolution molecular spectroscopy for producing ultracold absolute-ground-state $^{23}Na^{87}Rb$ molecules *Phys. Rev.* A **96** 052505

[93] Debatin M *et al* 2011 Molecular spectroscopy for ground-state transfer of ultracold RbCs molecules *Phys. Chem. Chem. Phys.* **13** 18926−35

[94] Yang A, Botsi S, Kumar S, Pal S B, Lam M M, Čepaitė I, Laugharn A and Dieckmann K 2020 Singlet pathway to the ground state of ultracold polar molecules *Phys. Rev. Lett.* **124** 133203

[95] Stein A, Knöckel H and Tiemann E 2008 Fourier-transform spectroscopy of Sr_2 and revised ground-state potential *Phys. Rev.* A **78** 042508

[96] Stein A, Knöckel H and Tiemann E 2010 The $^1S + {}^1S$ asymptote of Sr_2 studied by Fourier-transform spectroscopy *Eur. Phys. J.* D **57** 171−7

[97] McGuyer B H, Osborn C B, McDonald M, Reinaudi G, Skomorowski W, Moszynski R and Zelevinsky T 2013 Nonadiabatic effects in ultracold molecules via anomalous linear and quadratic Zeeman shifts *Phys. Rev. Lett.* **111** 243003

[98] Vitanov N V and Stenholm S 1999 Adiabatic population transfer via multiple intermediate states *Phys. Rev.* A **60** 3820

[99] Panda C D *et al* 2016 Stimulated Raman adiabatic passage preparation of a coherent superposition of the $H^3\Delta_1$ states for an improved electron electric-dipole-moment measurement *Phys. Rev.* A **93** 052110

[100] Yatsenko L, Shore B and Bergmann K 2014 Detrimental consequences of small rapid laser fluctuations on stimulated Raman adiabatic passage *Phys. Rev.* A **89** 013831

[101] Kondov S S, Lee C-H, Leung K H, Liedl C, Majewska I, Moszynski R and Zelevinsky T 2019 Molecular lattice clock with long vibrational coherence *Nat. Phys.* **15** 1118−22

[102] McDonald M, McGuyer B H, Iwata G Z and Zelevinsky T 2015 Thermometry via light shifts in optical lattices *Phys. Rev. Lett.* **114** 023001

[103] Han C, Zhou M, Zhang X, Gao Q, Xu Y, Li S, Zhang S and Xu X 2018 Carrier thermometry of cold ytterbium atoms in an optical lattice clock *Sci. Rep.* **8** 1−8

[104] Idziaszek Z and Julienne P S 2010 Universal rate constants for reactive collisions of ultracold molecules *Phys. Rev. Lett.* **104** 113202

[105] Jeziorski B and Moszynski R 1993 Explicitly connected expansion for the average value of an observable in the coupled-cluster theory *Int. J. Quantum Chem.* **48** 161−83

[106] Moszynski R, Żuchowski P S and Jeziorski B 2005 Time-independent coupled-cluster theory of the polarization propagator *Collect. Czech. Chem. Commun.* **70** 1109−32

[107] Korona T, Przybytek M and Jeziorski B 2006 Time-independent coupled cluster theory of the polarization propagator. Implementation and application of the singles and doubles model to dynamic polarizabilities and van der Waals constants *Mol. Phys.* **104** 2303−16

[108] Julienne P S and Tomza M (private communication).

[109] Christianen A, Zwierlein M W, Groenenboom G C and Karman T 2019 Photoinduced two-body loss of ultracold molecules *Phys. Rev. Lett.* **123** 123402

[110] Gregory P D, Blackmore J A, Bromley S L and Cornish S L 2020 Loss of ultracold $^{87}Rb^{133}Cs$ molecules via optical excitation of long-lived two-body collision complexes *Phys. Rev. Lett.* **124** 163402

[111] Chotia A, Neyenhuis B, Moses S A, Yan B, Covey J P, Foss-Feig M, Rey A M, Jin D S and Ye J 2012 Long-lived dipolar molecules and Feshbach molecules in a 3D optical lattice *Phys. Rev. Lett.* **108** 080405

[112] Ferrari G, Cancio P, Drullinger R, Giusfredi G, Poli N, Prevedelli M, Toninelli C and Tino G M 2003 Precision frequency measurement of visible intercombination lines of strontium *Phys. Rev. Lett.* **91** 243002